

ARTICLE TEMPLATE

Dislocation assisted coarsening of coherent precipitates: a phase field study

Arjun Varma R., Prita Pant and M. P. Gururajan

Department of Metallurgical Engineering and Materials Science, Indian Institute of Technology Bombay, Powai, Mumbai, Maharashtra India 400076

ARTICLE HISTORY

Compiled January 10, 2024

ABSTRACT

Coarsening of precipitates in coherent systems is influenced by the elastic fields of the precipitates and the interfacial curvature. It is also known that if precipitates are connected by dislocations, coarsening is affected by the elastic fields of the dislocations and the pipe diffusivity. Although there is experimental evidence of accelerated coarsening in the presence of dislocations, these studies do not capture the effect of the elastic fields. There exist generic theoretical models that can predict the average sizes and size distributions of coarsening precipitates considering the coherency related elastic stress fields. In this paper, we use a phase field model to study the coarsening of precipitates connected by dislocations, incorporating its elastic fields and pipe diffusivity. Specifically, we study the effects of misfit strain, elastic moduli mismatch, faster pipe mobility and the elastic fields of the dislocation on the morphology and kinetics of the coarsening precipitates. The dilatational component, associated with the edge character of the dislocations interact with the precipitates in an elastically homogeneous system. In an elastically inhomogeneous system, the deviatoric elastic fields also interact with the precipitates influencing the morphology and kinetics of coarsening precipitates. The kinetics of coarsening is different as well, with hard precipitates coarsening faster as compared to soft precipitates, when connected by dislocations. Further, we note that the modified Gibbs-Thomson equation, which was originally derived for an isolated precipitate in an infinite matrix, is also applicable for coarsening precipitates at close proximity.

KEYWORDS

Ostwald ripening; pipe diffusion; dissolution; misfit ; Gibbs-Thomson effect; capillarity

1. Introduction

The nucleation and growth of precipitates is followed by coarsening (or Ostwald ripening) during which larger precipitates grow at the expense of smaller precipitates; this is due to the Gibbs-Thomson effect which drives diffusion from regions of higher interfacial curvature to regions of lower interfacial curvature [1, 2]. The size distribution and the average size of the precipitates during coarsening is given by the LSW (Lifshitz-Slyozov-Wagner) theory [3, 4] albeit for the case when the volume fraction of the precipitates is very small. There exist modifications of this theory for finite volume fractions [5–9].

In the case of coherent precipitates, the interfacial equilibrium is also influenced by the elastic fields of the precipitates. Hence, Johnson has proposed an addition to the Gibbs-Thomson equation [10] to account for the effect of internal and external elastic fields of an isolated precipitate in an infinite system. Thus, in the case of coherent precipitates, the kinetics of coarsening is altered [10–12], and, at times, there is even inverse coarsening [12–15] where larger particles shrink and smaller particles grow.

Experimentally, it is known that several systems such as (but not limited to) Al–Li [16, 17], Cu–Fe [18, 19], Fe–Ti–C [20] and Fe–Cr [21] contain precipitates that remain coherent during coarsening, at least in the early stages. Dislocation activity in these systems result in dislocation glide towards the precipitates to minimise elastic energy and thereby connecting several precipitates. Such configurations may also be formed by the nucleation and growth of many precipitates on a dislocation line, which could act as a favourable site for precipitation [22–26].

When coherent precipitates and dislocations coexist, it is possible for the faster diffusivity of solutes along the dislocation core, known as “pipe diffusion”, to influence the coarsening behaviour of precipitates connected by them. There have been several experimental observations of accelerated coarsening of precipitates in the presence of dislocations [20, 27–35]. As opposed to the earlier studies which focused on an

average effect of the dislocations on coarsening, the study by Legros et al [32] is important in that they have focused on just two precipitates connected by a dislocation. By attributing the dissolution of the smaller precipitate entirely to pipe diffusion, they also estimate that the pipe diffusivity in the Al–Si system is about three orders of magnitude higher than the lattice diffusivity. But, the thin-film geometry of the samples used in these experiments largely eliminate the effect of the elastic fields, hence missing out an important aspect of interaction of the coarsening precipitates with the dislocation.

To summarise, there are theories that predict the average radius of particles and their size distributions in systems with coherent and incoherent precipitates. However, these studies do not account for pipe diffusion, or account for them as average effects, and neglect the elastic interaction between the dislocations and precipitates. On the other hand, there are experiments on the effect of pipe diffusion on coarsening; but, in these studies, the geometry is such that there is no appreciable elastic interaction between dislocations and coherency stresses and strains. Hence, in this paper, we consider the coarsening of coherent precipitates in the presence of dislocations while accounting for both the elastic interactions and the faster solute diffusion along the dislocations – albeit for the case of two precipitates. Given the intensity of the computations, development of parallel codes is needed to study large number of coherent precipitates in the presence of dislocations. Having said that, as we show below, a careful study and a deeper understanding of the effect of dislocations on coarsening of coherent precipitates is possible even in the case of two precipitates.

Phase field models have been used extensively to study phase transformation phenomena [36] and deformation [37]. Recently, the effect of dislocations on phase transformations has also been studied using phase field models by evolving the composition field in presence of stationary dislocations, while incorporating the elastic fields and pipe diffusion along the dislocations [38]. In this paper, using the same approach, we explore the effect of dislocations on the coarsening behaviour of two spherical precipitates of different sizes connected by them. Specifically, we study the effects of misfit strain, elastic moduli mismatch, faster pipe mobility and the elastic fields of the dislocations on the morphology and kinetics of coarsening of two precipitates. We

rationalise our simulation results in terms of the influence of the different parameters on the interfacial equilibrium, which, in turn, alters the morphology and kinetics.

This paper is organised as follows: in the next and following sections, we describe the phase-field model and the simulation details, respectively. In Sec. 4 we present our results on coarsening kinetics, and particle morphologies and rationalise the same using Gibbs-Thomson and modified Gibbs-Thomson equations. Finally, we conclude the paper with a summary of some key conclusions.

2. Phase-field model

We use a phase field model capable of capturing the evolution of the two phases of a binary system and the dislocations, using the field variables c and η . The model has been described in [38] and is a combination of the phase field dislocation dynamics model [39, 40] and the Cahn-Hilliard model for composition evolution [41]. The field variables c and η are evolved according to the Cahn-Hilliard and Allen-Cahn kinetics respectively and the total free energy of the system is composed of chemical, interfacial, elastic and core energy components:

$$F^{tot}(c, \eta) = N_V \int \left(A^{ch} c^2 (1 - c)^2 + \kappa |\nabla c|^2 \right) dV + \frac{1}{2} \int C_{ijkl}(c) \epsilon_{ij}^{el}(c, \eta) \epsilon_{kl}^{el}(c, \eta) dV + \sum_{\alpha=1}^N \int A^{core} \sin^2(\pi \eta_{\alpha}) dV \quad (1)$$

where N_V is the number of atoms per unit volume, A^{ch} is the bulk free energy coefficient that determines the height of the chemical energy barrier between the two phases, κ is the coefficient of interfacial energy, A^{core} is the coefficient of core energy and V is the total volume of the system. As indicated in eq. (1), the composition fields and the dislocations are coupled by their elastic fields; these elastic fields are, in turn, obtained by solving the equation of mechanical equilibrium,

$$\nabla \cdot \sigma^{el} = 0 \quad (2)$$

where σ^{el} is the elastic stress. Eq. (2) is solved using the Green's function approach [42]; we assume linear elasticity and carry out homogenization using an iterative technique as described in [43]. The modulus C_{ijkl} is considered a function of the composition c of the system, defined as:

$$C_{ijkl}(c) = C_{ijkl}^0 + \alpha(c)\Delta C_{ijkl} \quad (3)$$

where, we have taken $C_{ijkl}^0 = \frac{1}{2} [C_{ijkl}^m + C_{ijkl}^p]$ (an average of the matrix and precipitate moduli), $\Delta C_{ijkl} = C_{ijkl}^p - C_{ijkl}^m$ and $\alpha(c)$ is the interpolation function varying between 0 and 1 for $c = 0$ to $c = 1$, defined as: $\alpha(c) = [c^3 (10 - 15c + 6c^2) - \frac{1}{2}]$. The elastic fields for the system with the inhomogeneous moduli are obtained by an iterative method until the displacement fields converge, with mean error less than 10^{-8} ; see [43] for details.

In this study, as we are interested in the morphological evolution of coherent precipitates and their coarsening (dissolution of the smaller precipitate and growth of the larger precipitate), we evolve only the composition field. The dislocations are considered stationary in our simulations; the equilibrated configuration of dislocations is obtained by evolving the Allen-Cahn equation in the absence of the composition field; these configurations are used as the starting point for the coarsening simulations.

The faster pipe mobility along the core of the dislocations is implemented according to the variable mobility formulation of Zhu et al. [44]. The mobility M for a system containing N slip systems is given by:

$$M(\eta_\alpha) = M_b + M_f [\max(|\eta_1(1 - \eta_1)|, |\eta_2(1 - \eta_2)|, \dots, |\eta_N(1 - \eta_N)|)] \quad (4)$$

where $M_b = 1$ is the bulk mobility and M_f is the factor associated with the faster pipe mobility. In our simulations, we have taken $M_f = 400$, such that the peak mobility at the dislocation $M_{\text{peak}} = 101$. The pipe mobility term is highest when $\eta_\alpha = 0.5$, that is, at the dislocation core.

All parameters used in our simulations are non-dimensionalised (see [38] for details). The non-dimensionalised values of the key parameters of the model are shown in Ta-

Table 1. Non-dimensionalised values of parameters used in our simulations

Parameter type	Parameter	Value
Simulation	$\Delta x = \Delta y = \Delta z$	1.0
	δt	0.5 – 1.0
Free energy	A^{ch}	1.0
	A^{core}	1.0
Elastic	κ	1.0
	ϵ^c	0.01
	b	1.0
	$\frac{C_{1111}}{N_v}$	120
	$\frac{C_{1122}}{N_v}$	50
	$\frac{C_{1212}}{N_v}$	35
	Moduli contrast, δ	0.8, 1.0, 1.2
Allowed error in displacements	10^{-8}	

ble 1. We also consider two cases with an inhomogeneous elastic moduli; in those cases, the matrix moduli components are the same as that of the homogeneous, isotropic case in Table 1, and the precipitate moduli components are taken as 20 % higher and 20 % lower than those of the matrix phase.

3. Simulation details

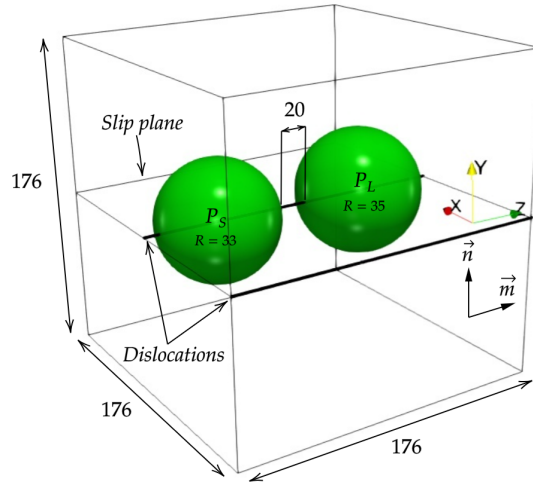


Figure 1. Simulation set-up consisting of two spherical precipitates (shown by green $c=0.5$ iso-surface) connected by a dislocation loop (shown in black). The slip plane in which the dislocation exists is shown. The system size is $176 \times 176 \times 176$. The directions of the slip plane normal (\vec{n}) and the sense vector (\vec{m}) are also indicated.

We consider a system of $176 \times 176 \times 176$ grid points; there are two spherical precipitates P_S (smaller) and P_L (larger) in this system which are connected by a straight dislocation line, as shown in Figure 1. In our simulations, in order to be consistent with the periodic boundary conditions, we consider an infinitely long (along z direc-

tion) straight dislocation dipole with one dislocation passing through the centre of the precipitates and the second dislocation situated on the xy face at a distance equal to half the simulation cell size: see Figure 1.

We consider the following cases of simulations for our study:

- (1) CC (**C**oarsening due to interfacial **C**urvature)
- (2) CCE (**C**oarsening driven by interfacial **C**urvature and **E**lastic fields)
- (3) CCI (**C**oarsening due to interfacial **C**urvature and elastic fields in an elastically **I**nhomogeneous system)
- (4) CCED (**C**oarsening driven by interfacial **C**urvature and **E**lastic fields in the presence of a connecting **D**islocation). The dislocations affect the coarsening in the following two ways:
 - (a) The mobility is faster (pipe mobility) along the dislocation line.
 - (b) The elastic fields of the dislocation interact with those of the solutes.
- (5) CCID (**C**oarsening due to interfacial **C**urvature and elastic fields in an elastically **I**nhomogeneous system in the presence of **D**islocations)

We consider isotropic elastic moduli for both the precipitate and the matrix in all cases. The initial radii of P_S and P_L are fixed at 33 and 35 non-dimensionalised length units (for the small and large precipitate, respectively) and the surface to surface distance (measured along the z direction) is equal to 20 units. In order for the precipitates to be stable and not shrink, we need to maintain corresponding supersaturation in the matrix. In all cases, we maintain a supersaturation that will support the smaller precipitate. However, this supersaturation value will make the bigger precipitate to grow. Hence, the difference in radii between the two precipitates is kept to a minimum to ensure that there is negligible amount of supersaturation for P_L and the increase in its volume occurs primarily at the expense of P_S . The results for the CC and the CCE cases are presented from $t=10000$ onwards in order to avoid the initial transients and compositional adjustments. The composition profile at $t=10000$ from the CCE (CCI) case is used as the initial composition profile in the case of the CCED (CCID) simulations.

4. Results and discussion

In all the cases, we present the precipitate volume fraction as a function of time (which stays nearly a constant since we are in the coarsening regime), the change in the individual precipitate sizes with time (P_S shrinks while P_L grows), and the morphological changes, if any; in all cases, we also show and discuss the Gibbs-Thomson effect. We use the Case CC as the baseline for discussing all the subsequent simulation results.

4.1. Case CC: Effect of interfacial curvature

We begin the simulations with a far-field composition $c_f = 0.0101$, since this is the equilibrium composition at the interface corresponding to the spherical precipitate P_S of radius 33 units, obtained using the Gibbs-Thomson equation [10] (see Supplementary information for calculation):

$$\Delta c_{int}^m = \frac{2\gamma\chi^p}{(c_\infty^p - c_\infty^m)\Psi_m} \quad (5)$$

where γ is the interfacial energy of the system, χ^p is the mean curvature of the precipitate with respect to the precipitate phase, and c_∞^p, c_∞^m are the equilibrium compositions of the matrix (zero for the double well potential assumed by us) and precipitate (unity for the double well potential assumed by us) phases respectively when separated by a flat interface (that is, $R \rightarrow \infty$). Ψ_m is the curvature of the bulk free energy density versus composition curve, calculated at c_∞^m . Note that the interfacial equilibrium compositions at the matrix and precipitate sides of the curved interface Δc^m and Δc^p are also equal for the double well potential, as the curvatures of bulk free energy densities Ψ_m and Ψ_p , calculated at c_∞^m and c_∞^p respectively, are equal. In the same way, we take the initial compositions of the precipitates P_S and P_L as 1.0101 and 1.0095, respectively.

In Figure 2, we show the the total volume of the precipitates and the effective radius of the two precipitates as a function of time. The effective radii of the precipitates are

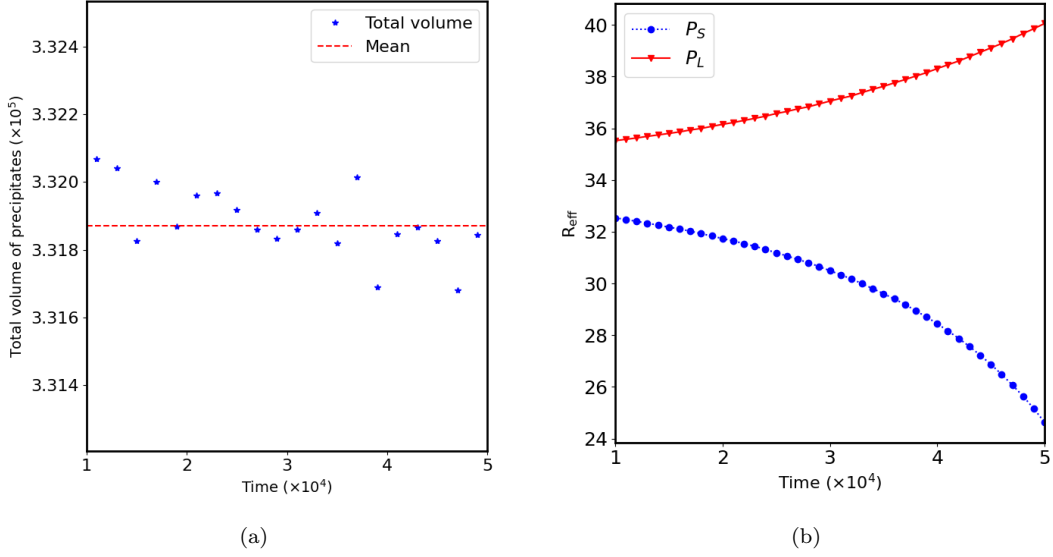


Figure 2. Variation of (a) total volume of precipitates with time and (b) R_{eff} of smaller (P_S) and larger (P_L) precipitates with time. Both profiles are shown only from $t=10000$, after the initial adjustments.

calculated as:

$$R_{\text{eff}} = \left(\frac{3V}{4\pi} \right)^{\frac{1}{3}} \quad (6)$$

where V is the volume of the precipitate, obtained by counting the number of grid points with $c \geq 0.5$. The total volume of the precipitate remains constant throughout the simulation; note that the oscillations seen are an artifact of the way in which the volume fraction is estimated. The effective radius of the smaller precipitate decreases and the larger precipitate increases. Hence, it is clear that the precipitate size changes are due to coarsening.

The composition profile of the smaller precipitate (P_S) is plotted at different stages of evolution in Figure 3 (a). Due to Gibbs-Thomson effect, the equilibrium composition inside the precipitate c_R^p increases as the R_{eff} of P_S decreases. In Figure 3 (b), the $\Delta c_{\text{int}}^p = c_R^p - c_\infty^p$ at P_S is plotted against the inverse of R_{eff} ; since the precipitate remains spherical, inverse of R_{eff} is nothing but the mean curvature (χ^p) of the precipitate-matrix interface. According to equation (5), a linear fit of Δc_{int}^p against χ^p should yield a slope equal to the interfacial energy γ and a zero intercept. The slope obtained from our fit is 0.33, which is close to the interfacial energy $\gamma = \frac{1}{3}$ for our

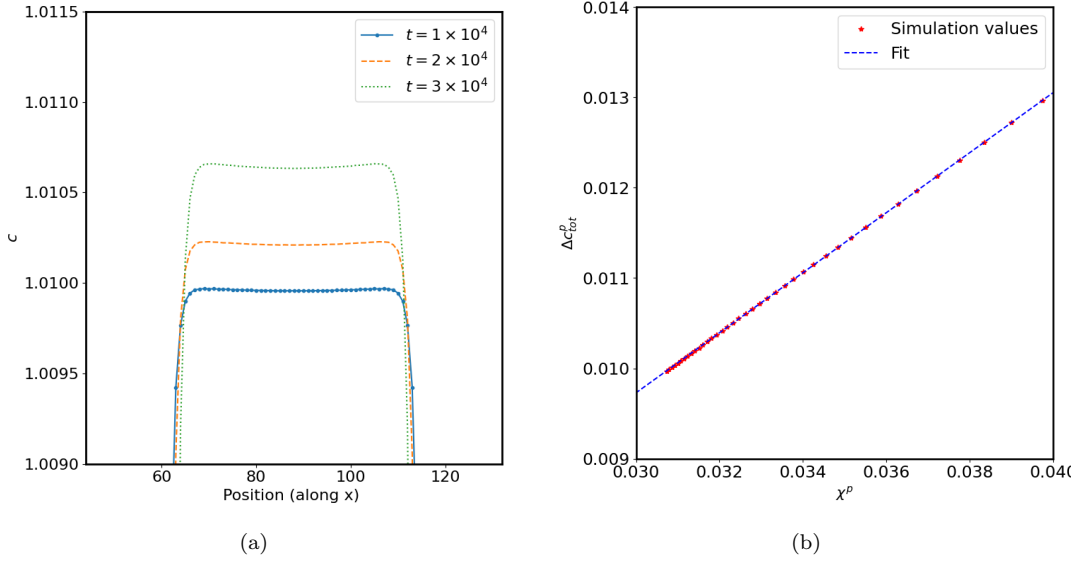


Figure 3. (a) Composition profile of smaller precipitate P_S (plotted along the x -direction) increases as R_{eff} decreases. (b) The fit of $\Delta c_{\text{int}}^p = c_R^p - c_\infty^p$ against mean curvature χ^p (dotted line) superimposed on the values obtained from the simulations. The fit has $R^2 = 1$ and a residual standard error of 4.49×10^{-6} . The standard errors associated with the slope and intercept are respectively equal to 2.544×10^{-4} and 8.592×10^{-6} .

choice of A^{ch} and κ . Further, the intercept of the fitted line is equal to -0.0002, close to the expected value of zero. The same exercise was also repeated for the precipitate P_L for which the slope and intercept were respectively equal to 0.33 and -0.0004. The agreement of the values obtained from the fit with the theoretically calculated values serves as a benchmark for our code.

4.2. Case CCE: Effect of precipitate coherency

In these simulations, the far-field composition is taken to be $c_f = 0.0165$. This is equal to the equilibrium interfacial composition for the smaller precipitate (P_S of radius 33) when the magnitude of misfit strain $\epsilon^c = 0.01$. This is calculated according to the modified Gibbs-Thomson equation, which incorporates the effect of elastic fields of the precipitates [10] (the second term in the following equation):

$$\Delta c_{tot}^m = \frac{2\gamma\chi^p}{(c_\infty^p - c_\infty^m)\Psi_m} + \frac{\sigma_{ij}^m(\epsilon_{ij}^m - \epsilon_{ij}^p) + \frac{1}{2} \left[\sigma_{ij}^p(\epsilon_{ij}^p - \epsilon^c \delta_{ij}) - \sigma_{ij}^m \epsilon_{ij}^m \right]}{(c_\infty^p - c_\infty^m)\Psi_m} \quad (7)$$

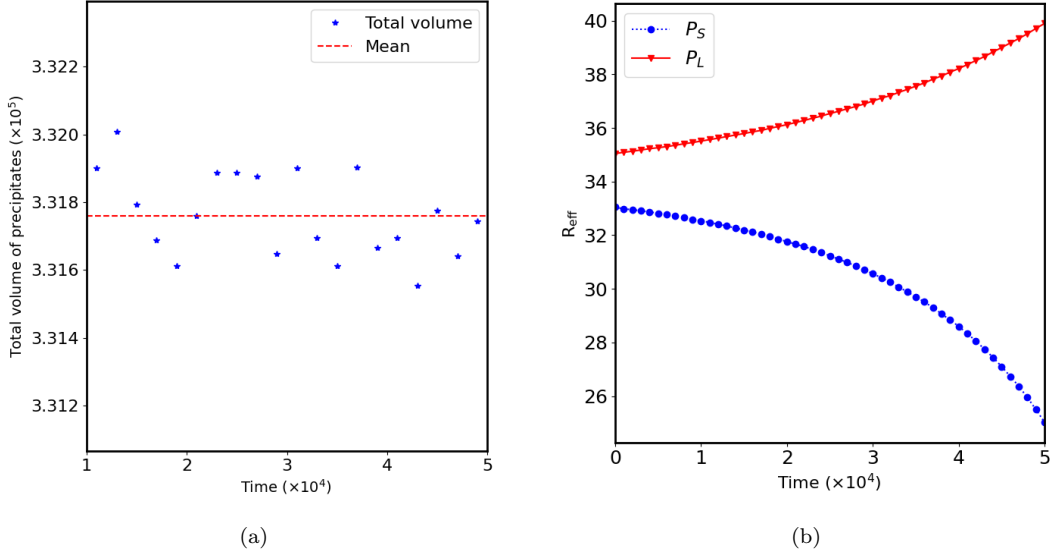


Figure 4. Variation of (a) total volume of precipitates with time (red line is the mean) and (b) R_{eff} of smaller (P_S) and larger (P_L) precipitates with time for the CCE case.

where σ^m , σ^p and ϵ^m , ϵ^p are the stresses and total strains at the matrix and precipitate sides of the interface and ϵ^c is the magnitude of the misfit strain of the precipitate. (see Supplementary information for calculation.)

Figure 4 shows the evolution of the total volume of the two precipitates and the radius of each precipitate respectively, clearly showing that the system is within the coarsening regime. In Figure 5, we show the equilibrium composition inside the smaller precipitate (P_S) at different time steps time and a linear fit of $\Delta c_{\text{tot}}^p = c_R^p - c_\infty^p$ against the mean curvature $\chi^p (= \frac{1}{R_{\text{eff}}})$. As the radius of the smaller precipitate P_S decreases, the equilibrium composition within the precipitate (c_R^p) becomes higher. The linear fit yields a slope equal to 0.32 and a y -intercept equal to 0.0053. In the CCE case, the y -intercept is equal to the second term in eq. (7), that is the elastic contribution to Δc_{tot}^p . The elastic contribution Δc_{el}^p may also be calculated by obtaining the elastic fields of the precipitate by solving Eshelby's inclusion problem [42]. The value of Δc_{el}^p obtained using this approach is equal to 0.0064. We believe that this difference in intercepts is due to the elastic field overlap of the two precipitates and hence the Eshelby solution which is meant for the isolated precipitate has to be corrected by including this elastic interaction.

Hence, in order to rationalise this difference between the value obtained from the

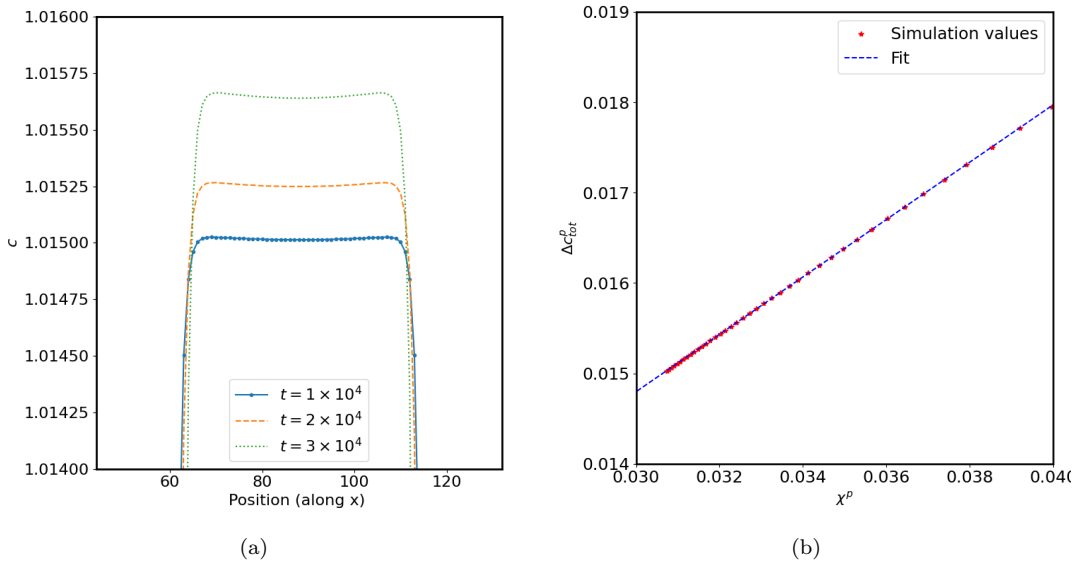


Figure 5. (a) Composition profiles plotted along the x direction of smaller precipitate at different timesteps shows an increase in equilibrium composition of precipitate with a decrease in size of the precipitate. (b) A linear fit of $\Delta c_{tot}^p = c_R^p - c_\infty^p$ against mean curvature $\chi^p = \frac{1}{R_{eff}}$ produces a y-intercept of 0.0053. The fit has $R^2 = 1$ and a residual standard error of 3.51×10^{-6} . The standard errors associated with the slope and intercept of the fit are respectively 2.178×10^{-4} and 7.321×10^{-6} .

simulation and theory, we carried out a finite-size scaling analysis by varying the interparticle distance. Figure 6 shows the Δc_{el}^p contribution at different interparticle spacings. There is an increase in the value of Δc_{el}^p as the interparticle spacing increases. A linear fit of Δc_{el}^p values against the inverse of interparticle spacing ($\frac{1}{r_p}$) yields a y-intercept of 0.0062, close to the theoretically calculated value. Hence, the difference in Δc_{el}^p from our simulations with respect to the theoretical calculation may be attributed to the interaction between the precipitates.

It is also worth noting that the elastic fields of a precipitate are independent of the size of the precipitate [10]. Hence, the Δc_{el}^p contributions for both precipitates remain the same in the case of CCE simulations. Hence, the concentration gradient between the two precipitates should remain the same for CC and CCE cases, resulting in same kinetics of evolution. The difference in evolution kinetics between the two cases is minimal, as expected, and the minor difference is due to the slightly larger supersaturation for smaller precipitate (P_S) in the CCE case ($c_f = 0.0165$), which was calculated by taking Δc_{el}^p equal to the theoretically calculated value of 0.0064 (see Supplementary information).

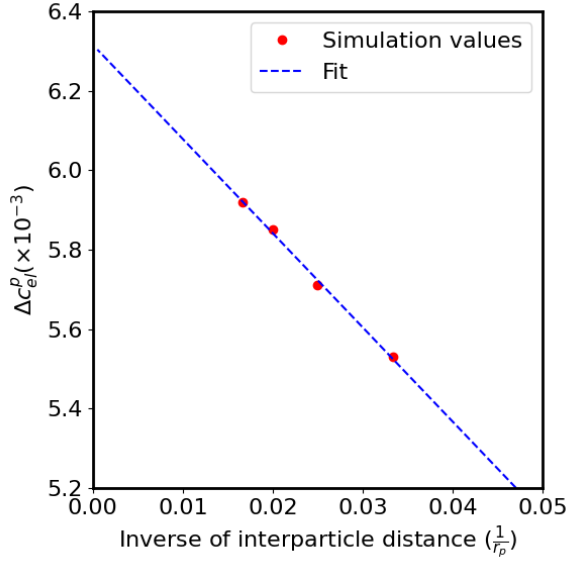


Figure 6. Finite-size scaling of Δc_{el}^p against the inverse of inter-particle separation ($\frac{1}{r_p}$). The inter-particle separations of 30, 40, 50 and 60 units are obtained in grids of size 196^3 , 216^3 , 236^3 and 256^3 respectively. The y -intercept (corresponding to a Δc_{el}^p at infinite interparticle spacing) is 0.0063. The fit has $R^2 = 0.9963$ and a residual standard error of 1.252×10^{-5} . The standard errors associated with the slope and the intercept of the fitted line are respectively 9.94×10^{-5} and 2.45×10^{-5} .

4.3. Case CCED (a): Effect of pipe diffusivity of dislocation

Next, we consider the effect of dislocations, but only due to the faster pipe diffusion along the dislocation core. In the study by Legros et al [32], the dissolution of the smaller precipitate was assumed to occur only by virtue of pipe diffusion through the dislocation. However, for our simulations, such an assumption would be incorrect. Hence, a direct comparison of our results with the experiment is not possible, as diffusion occurs both through the dislocation core and the bulk. So, we calculate the apparent mobility of the system due to the introduction of the dislocations in the system.

In order to obtain the apparent atomic mobility, we follow the definition of apparent diffusivity in [1]:

$$D_{\text{app}} = D_{\text{lattice}} + a_f D_{\text{pipe}} \quad (8)$$

where D_{lattice} is the diffusivity in the defect free lattice, a_f is the area fraction and D_{pipe} is the diffusivity through the dislocation pipe. By definition, the atomic mobility

and diffusivity are related as $D = M\Psi$, where $\Psi = \frac{\partial^2 f}{\partial c^2}$ is the curvature of the double well potential. Hence, eq. (8) will approximate for atomic mobility as well, as Ψ is the same on both sides and hence can be cancelled out. In our simulations, the pipe mobility is defined according to eq. (4), which peaks at the dislocation line and drops down to the bulk mobility value in a diffuse manner (see supplementary information). For the choice of our parameters, the peak value of mobility is equal to $M_{\text{peak}} = 101$, two orders of magnitude higher than the mobility in the bulk. However, as the mobility is varying in a diffuse manner between these values, we have adopted the following definitions for M_{lattice} , M_{pipe} , and a_f . We consider a plane perpendicular to the slip plane, which is also perpendicular to the dislocation line, as shown in Figure 7.

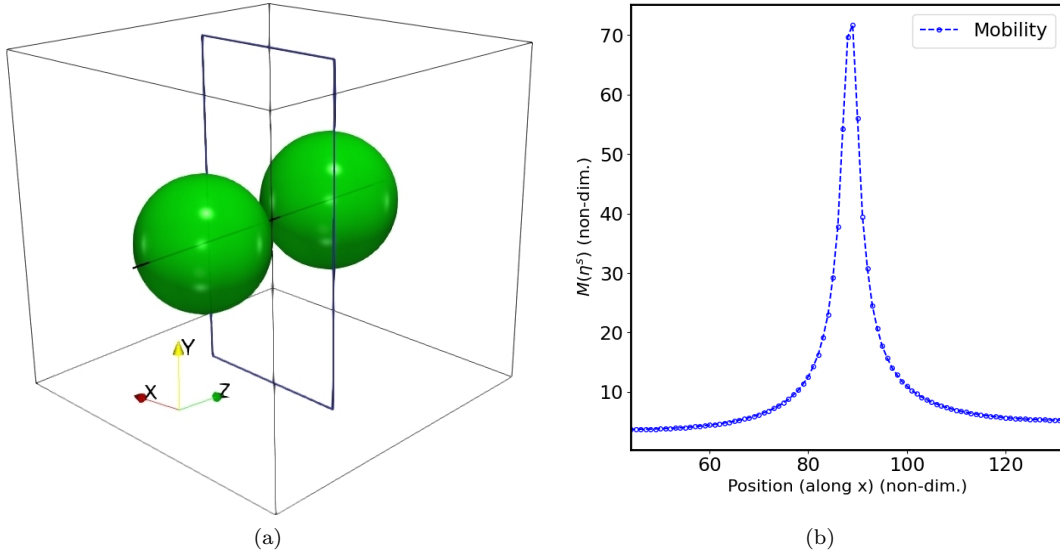


Figure 7. Schematic of (a) the xy plane between the two precipitates used for calculating the area fraction of the pipe and the flux along the z -direction. (b) Position dependent mobility plotted along a line taken in the slip plane and perpendicular to the line direction of the dislocations. (See supplementary information for a 2D map of position dependent mobility perpendicular to the slip plane.)

Next, we define the dislocation pipe to be the grid points on this plane, where $M \geq \frac{M_{\text{peak}}}{10}$ and the grid points where $M < \frac{M_{\text{peak}}}{10}$, as the bulk region. The average mobility of all points in the pipe region was taken as M_{pipe} and that of all points outside of this region was taken as M_{lattice} . The area fraction of the pipe was calculated as the fraction of grid points on the plane within the pipe region. The value $\frac{M_{\text{peak}}}{10}$ is chosen to define the pipe region as the mobility outside this region may be considered almost invariant.

Using this method for calculation, we obtain $M_{\text{lattice}} = 2.031$, $M_{\text{pipe}} = 17.91$ and $a_f = 0.00464$. Hence, the apparent mobility of the system for our choice of parameters is:

$$\begin{aligned} M_{\text{app}} &= M_{\text{lattice}} + a_f M_{\text{pipe}} \\ &= 2.031 + 0.00464 \times 17.91 \\ &= 2.114 \end{aligned} \tag{9}$$

It is also possible to calculate M_{app} by taking the ratio of the flux across the plane in Figure 7 from the smaller to the larger precipitate in the z -direction. This is because the pipe diffusion does not alter the energetics of the system and hence the driving force for diffusion remains the same in both cases. The flux is calculated as:

$$J_z = -N_v M \left[\frac{\partial \mu^{\text{tot}}}{\partial z} \right] \tag{10}$$

where M is the atomic mobility of the system (position dependent for the case CCED (a)), $\frac{\partial \mu^{\text{tot}}}{\partial z}$ is the gradient in the total potential along the z -direction, where $\mu^{\text{tot}} = \left(\frac{1}{N_v} \frac{\delta F^{\text{tot}}(c, \eta^\alpha)}{\delta c} \right)$ is the variational derivative of the total free energy of the system with respect to composition. Hence, the ratio of the fluxes calculated in the CCE and CCED (a) case is expected to give the apparent mobility M_{app} (because $M = 1$ in CCE case). Table 2 shows the fluxes calculated for the two simulation cases and the apparent mobility, obtained as the ratio of the two fluxes, at different effective radii of the smaller precipitate P_S .

Table 2. Apparent mobility of CCED(a) case keeping CCE case as the reference.

R_{eff} of P_S	J_z (CCE)	J_z (CCED)	M_{app}
32	0.46	1.01	2.19
30	0.80	1.80	2.25
28	1.10	2.41	2.19
26	1.35	2.92	2.16

The M_{app} value obtained by taking the ratio of the fluxes from the two simulation cases agree well with the value obtained from the calculation based on eq. (8), indicating that the accelerated diffusion kinetics along the dislocation is correctly captured

in our simulations.

4.4. Case CCED (b): Effect of elastic fields of dislocation (along with pipe diffusivity)

Next, we consider the results from the CCED case incorporating the strain fields of the dislocations. In Figure 8, we show the xy , yz and xz sections of the smaller precipitate (P_S) at time $t=12500$ for the screw and edge type connecting dislocations respectively.

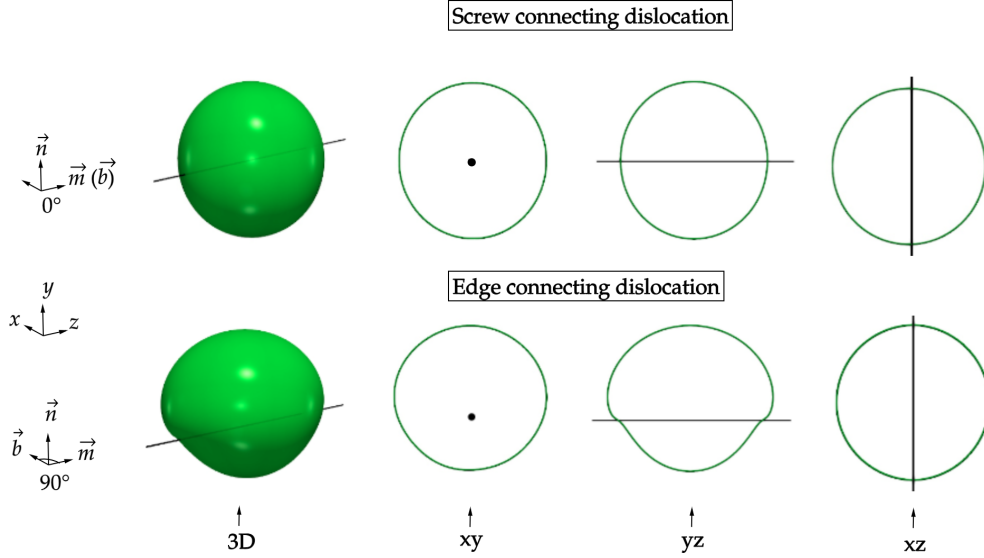


Figure 8. Morphology of smaller precipitate P_S connected by screw (first row) and edge (second row) dislocations at $t=12500$

The screw connecting segment, which only has deviatoric elastic field components (for linear elasticity), does not interact with the purely dilatational strain field of the precipitate. Due to this, the shape of the precipitate is not affected by the elastic interaction. Hence, the morphology of the precipitates with screw connecting dislocation is identical to the morphology in the CCED (a) case, considering only pipe diffusivity of the dislocation.

However, for the edge connecting dislocation, interaction between the dilatational components of the dislocation and the elastic fields of the precipitate results in significant change of shape of the precipitate. The unfavourable elastic fields below the slip plane causes material to flow to above the slip plane, locally along the precipitate surface. Due to this, the precipitates develop a protrusion parallel to the dislocation

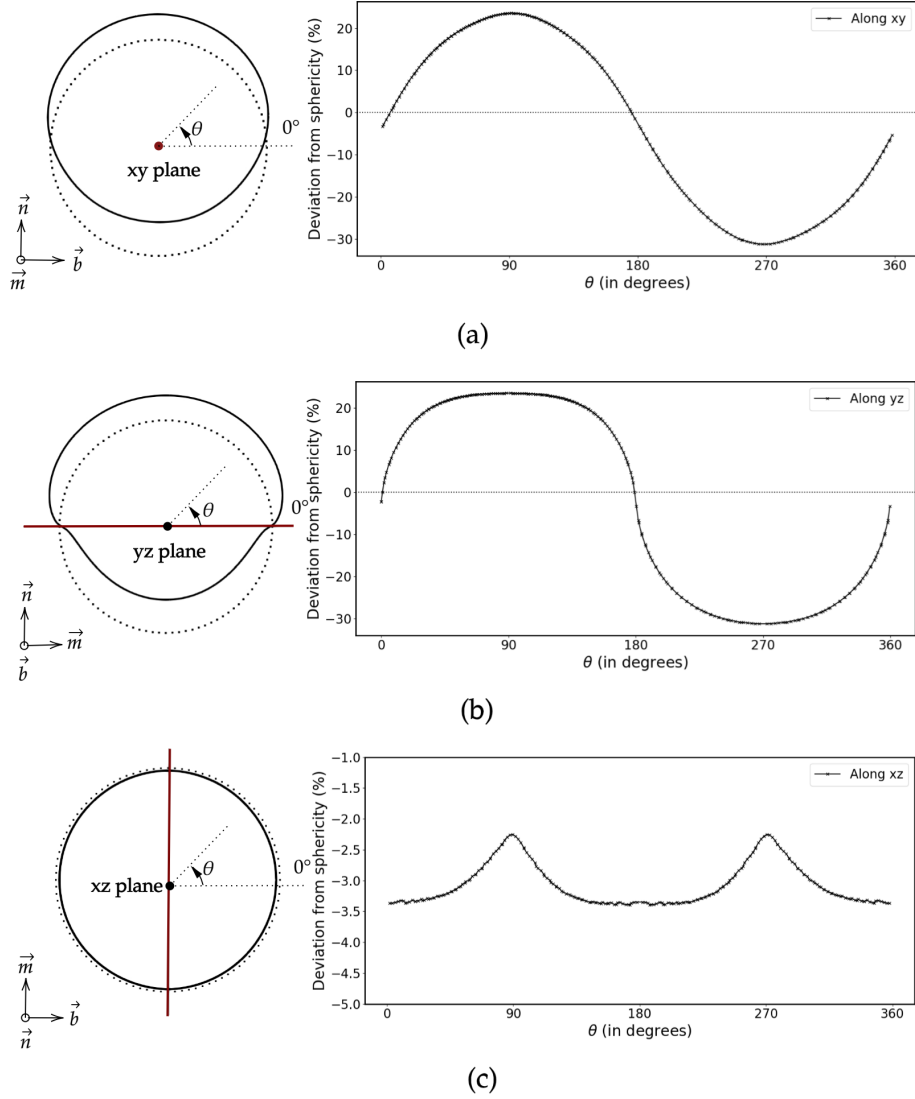


Figure 9. The % deviation (from spherical shape) of the morphology of the smaller precipitate P_S connected by an edge dislocation. The deviation is measured by taking the radial distance between the two profiles as a fraction of the radius of the sphere.

line above the slip plane, as clearly seen from the yz section of P_S in the second row in Figure 8.

For the edge dislocation case, the deviation from sphericity of P_S is calculated by taking the radial distance of the precipitate section from a coincident sphere and is expressed as a fraction of the radius of this sphere, for different angles about the horizontal, as shown in Figure 9. The deviation is considered positive if the portion of the precipitate is lying outside the sphere and negative otherwise. The movement of material from below the slip plane to above is clearly visible in the xy and yz

sections. The formation of a protrusion along the dislocation line (z -direction) is also observed, indicating a change in the local curvature, which is expected to alter the local equilibrium interfacial composition.

As there is a significant change in the shape of the precipitate from the initial spherical shape, it is not possible to calculate the Δc_{el}^p for the CCED cases by fitting Δc_{tot}^p against the mean curvature (χ^p). Since the mean curvature (χ^p) would be different at different points on the surface of the precipitate, we consider six points on the precipitate surface, three above and three below the slip plane, as shown in Figure 10, where the Δc_{tot}^p is calculated using the stress and strain fields and the mean curvature of the interface calculated at those points using the parallel surface method [45]. These values are then compared with the Δc_{tot}^p obtained from the composition profile, thus checking the applicability of the modified Gibbs-Thomson equation in predicting the changed interfacial equilibrium due to the dislocations. As the dislocation eigenstrain is discontinuous along the y -direction, the elastic fields calculated by FFT method oscillate due to Gibbs phenomenon. Hence, the stress and strain fields are smoothed by taking a five-point average along the y -direction.

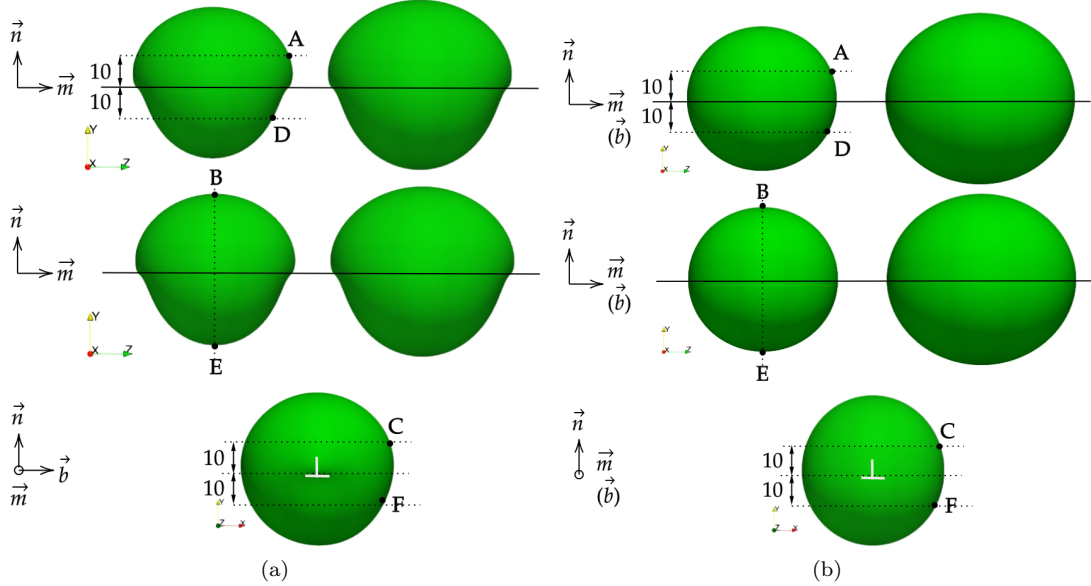


Figure 10. Points on the surface of precipitate connected by (a) edge and (b) screw dislocations at which Δc_{tot}^p is calculated using modified Gibbs-Thomson equation.

The values of Δc_{tot}^p calculated at the six points for the two types of dislocations, along with the value obtained from the composition profiles and the % relative error

is tabulated in Table 3. There is a broad agreement between the values obtained by calculations based on the modified Gibbs-Thomson equation and the equilibrium composition read from the composition profile. The difference is of the order of 10% which may be attributed to two factors: (a) the error in the calculation of mean curvature (χ^p) using the parallel surface method (PSM) [45], and (b) the assumption made while deriving the modified Gibbs-Thomson equation that farfield composition (c_f) remains a constant, which is not fully satisfied in our simulations due to the limitations in system size.

Table 3. Δc_{tot}^p contributions from elastic and interfacial terms calculated by substituting the stress and strain fields at different points on the precipitate in the modified Gibbs-Thomson equation and compared with the equilibrium composition from the composition profile at the same point. The values for three cases: namely (a) without dislocation, (b) screw and (c) edge type dislocations are tabulated.

Point	From modified G-T equation			Δc_{tot}^p from comp. profile	% error
	Δc_{el}^p (1)	Δc_{int}^p (2)	Δc_{tot}^p (1)+(2)		
No dislocation					
A	0.00554	0.01069	0.0162	0.0150	8
B	0.00531	0.01109	0.0164	0.0150	9
C	0.00572	0.01064	0.0164	0.0150	9
D	0.00552	0.01069	0.0162	0.0150	8
E	0.00529	0.01109	0.0164	0.0150	9
F	0.00571	0.01064	0.0164	0.0150	9
Screw					
A	0.00547	0.01075	0.0162	0.0150	8
B	0.00528	0.01123	0.0165	0.0150	10
C	0.00574	0.01084	0.0166	0.0150	11
D	0.00555	0.01075	0.0163	0.0150	9
E	0.00524	0.01123	0.0165	0.0150	10
F	0.00575	0.01084	0.0166	0.0150	11
Edge					
A	-0.000547 [†]	0.01657 [†]	0.0160	0.0146	10
B	0.00427	0.01030	0.0146	0.0133	10
C	0.00481	0.01150	0.0163	0.0149	9
D	0.01169 [†]	0.00487 [†]	0.0166	0.0154	8
E	0.00593	0.01220	0.0181	0.0163	11
F	0.00660	0.01030	0.0169	0.0155	9

[†] The values marked show an order of magnitude difference in the elastic contribution Δc_{el}^p and its effect on the interfacial contribution Δc_{int}^p in the case of edge dislocation.

Another important point is the order of magnitude difference in the Δc_{el}^p contribution (marked with [†] symbol in the table) between the points A and D. This is due to the elastic fields of the dislocation which is equal in magnitude but opposite in direction above and below the slip plane. This difference causes material flow from below to above the slip plane, forming a protrusion above the slip plane along the direction of the dislocation line and hence, a larger mean curvature (χ^p) at A as compared to D. Hence, the elastic fields of the dislocation does not only change the elastic con-

tribution of the modified Gibbs-Thomson equation, but also influences the curvature contribution.

4.5. Case CCID: Effect of dislocations in elastically inhomogeneous systems

Next, we consider the effect of elastic inhomogeneity of the system, by considering two sets of simulations with precipitate moduli 20 % higher ($C^p = 1.2C^m$) and 20 % lower ($C^p = 0.8C^m$) compared to the matrix phase, for the edge and screw connecting dislocations. In Figure 11, we show the superimposed xy , yz and xz sections of the hard and soft precipitate for the edge and screw connecting dislocations at $R_{\text{eff}} = 28$. There is a marked difference in the shape of the hard and soft precipitates while connected by the same dislocation type. In the case of the edge connecting dislocation, the rate of material transport from below to above the slip plane is faster in the case of the hard precipitate, as clearly seen in the xy and the yz sections. The protrusion formed along the direction of the dislocation line – due to the material flow from below to above the slip plane – is more pronounced for the soft precipitate than the hard precipitate, which is evident from the yz and xz views on the first row. Even for the case of screw dislocation, there is a localised shape change near the dislocation line, with a protrusion occurring for the soft precipitate at the point of exit of the dislocation from the precipitate, and a dent on the surface, at the vicinity of the dislocation, for the hard precipitate.

Unlike the CCED (b) case, there is an interaction of the elastic field of the precipitate with the (purely deviatoric) elastic fields of the screw dislocation, causing a shape change. In an inhomogeneous system, the elastic energy integral can be expanded and the elastic component of the driving force can be obtained by taking its variational derivative as follows [46]:

$$\begin{aligned} \frac{\delta \left[\frac{F^{\text{el}}}{N_V} \right]}{\delta c} &= -C_{ijkl}^{0r} \epsilon^c \delta_{ij} \beta'(c) (E_{kl} + \epsilon_{kl}^* - \sum_{s=1}^{N_s} \epsilon_{kl}^{0d}(\eta^s) - \epsilon_{kl}^{0c}(c)) + \\ &\alpha'(c) \Delta C'_{ijkl} (E_{ij} + \epsilon_{ij}^* - \sum_{s=1}^{N_s} \epsilon_{ij}^{0d}(\eta^s) - \epsilon_{ij}^{0c}(c)) (E_{kl} + \epsilon_{kl}^* - \sum_{s=1}^{N_s} \epsilon_{kl}^{0d}(\eta^s) - \epsilon_{kl}^{0c}(c)) \quad (11) \end{aligned}$$

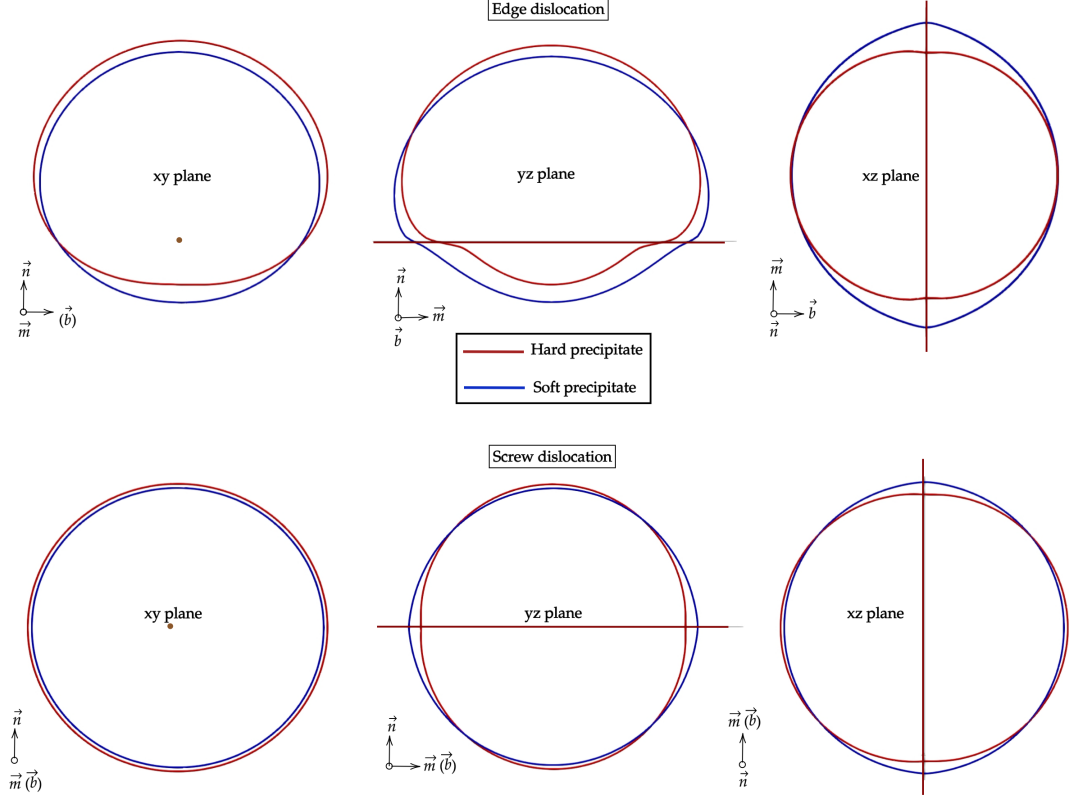


Figure 11. Morphology of the smaller precipitate P_S connected by edge (top row) and screw (bottom row) dislocations respectively.

where $C_{ijkl}^{0r} = \frac{C_{ijkl}^0}{N_v}$, $\Delta C'_{ijkl} = \frac{\Delta C_{ijkl}}{N_v}$, $\alpha(c)$ and $\beta(c)$ are interpolating functions, E_{ij} is the homogeneous (macroscopic) strain tensor, ϵ_{ij}^* is the periodic (microscopic) strain, and, ϵ^{0c} and ϵ^{0d} are the eigenstrains associated with the composition and dislocation fields. The first term on the right hand side of eq. (11) is identical for homogeneous and inhomogeneous systems, with the exception of the value of C_{ijkl}^{0r} used. There is no contribution due to the deviatoric elastic fields in the first term, due to the presence of δ_{ij} resulting from the derivative of ϵ^{0c} (following the assumption that precipitate elastic fields are purely dilatational). Note that the sign of this term is also negative. The second term is present only in the case of inhomogeneous systems, and does not reduce to zero for deviatoric fields. Moreover, all variables except for $\Delta C'_{ijkl}$ are positive. $\Delta C'_{ijkl}$ is positive (negative) for $C^p > C^m$ ($C^p < C^m$) and hence, the second term will counteract (augment) the first term for the hard (soft) precipitate. Due to this, there is a gradient in the elastic potential which moves material away from the dislocation for the hard precipitate and towards the dislocation line for the soft precipitate. As

the deviatoric fields are highest near the dislocation lines and decreasing away from it, this causes the formation of the protrusion at the surface of the soft precipitate and the depression at the surface of the hard precipitate close to the dislocation, in the case of screw dislocation. The variation in morphology for hard and soft precipitates with edge connecting dislocations is also due to their interaction with the deviatoric elastic field of the edge connecting dislocation.

Further, we also performed the calculation of the Δc_{tot}^p at the points A to F similar to the CCED (with elastic fields and pipe diffusivity) simulations. In this case also, there is a broad agreement of the equilibrium composition values calculated from the modified Gibbs-Thomson equation with that obtained from the composition profile, suggesting that the modified Gibbs-Thomson equation is applicable in this case as well.

4.6. Comparison of rates of coarsening

Finally, we make a comparison of the coarsening rates of the different simulation cases. In Figure 12, we show a comparison of the effective radius R_{eff} for the smaller precipitate for the CC, CCE and CCED(a) cases, showing the effect of pipe diffusivity on the rate of coarsening.

The coarsening rates for the CC and the CCE cases are almost identical in our simulations. It has been shown that the elastic fields of a coherent precipitate are independent of the size of the precipitate [47]. Hence, the elastic contribution to the Gibbs-Thomson effect is the same outside both precipitates, leaving the concentration gradient between them unaffected. Note that they are not exactly identical due to the slightly larger supersaturation of P_S in the CCE case for $c_f = 0.0165$, as shown by our finite size scaling analysis. The faster pipe diffusion along the dislocation accelerates the kinetics for the CCED(a) case.

We show the evolution of effective radius for the CCED(b) case in Figure 13. The kinetics of coarsening is the same for the screw connecting dislocation as compared to the CCED(a) case (with only pipe diffusivity), as the deviatoric strain fields of the screw dislocation do not interact with the dilatational misfit strain fields of the precipitates. Also, the kinetics is slower in the case of the edge dislocation, as shown in

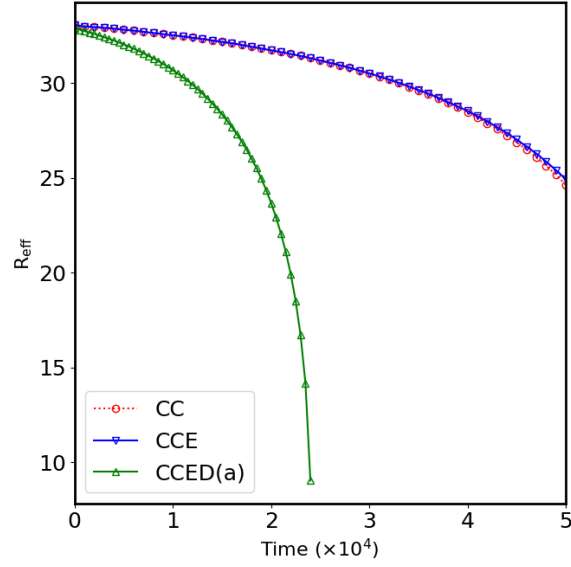


Figure 12. R_{eff} as a function of time for CC, CCE and CCED(a) cases. The coarsening rates are almost identical for the CC and CCE cases as the elastic fields of the precipitates are independent of the size. The coarsening rates for the CCED case is faster due to pipe diffusion. The timescale starts at $t=0$ corresponding to the CCED(a) case, after initial adjustments, and the comparison is made with corresponding timesteps from the CC and CCE cases.

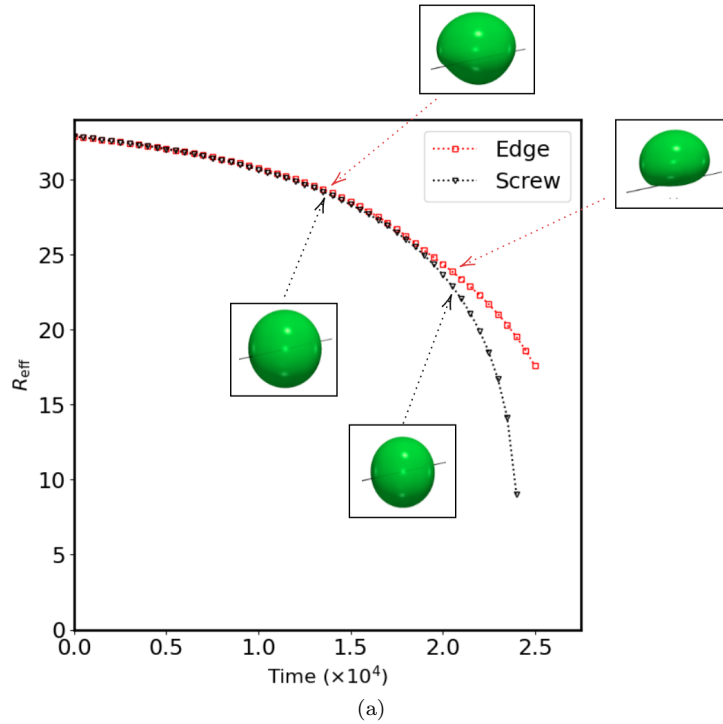


Figure 13. The evolution effective radius R_{eff} for the edge and screw dislocation cases (CCED (b)) along with the morphology of the precipitates shown for $t=12500$ and $t=20000$. The insets indicated by red arrows correspond to the edge type connecting dislocation and the black arrows correspond to the screw type connecting dislocation.

Figure 13, as the solutes in the precipitate find the dislocation elastic fields above the slip plane to be favourable as compared to below the slip plane, setting up a flux from below to above the slip plane. The subsequent shape change due to this flux causes a change in the equilibrium interfacial compositions of the two precipitates, reducing the concentration gradient. This makes the kinetics of coarsening slower in the case of the edge dislocations.

We show the effect of elastic inhomogeneity on coarsening rates in Figure 14. In Figure 14(a), we compare the CCE and CCI cases, which are the cases of coherent precipitates without dislocations. It is clear that the coarsening rates are unaffected by the modulus ratio between the precipitates and matrix phases. In an elastically inhomogeneous system, even though the elastic fields of a precipitate are a function of its shape, as the smaller and larger precipitates both have a spherical shape, the Δc_{el}^p contribution to the interfacial equilibrium composition is the same for P_S and P_L . Hence, the composition gradient between the precipitates is only a function of the interfacial curvature of the precipitates for CCE and CCI, giving them identical coarsening kinetics. In the CCI case, we had used $c_f = 0.0175$ and $c_f = 0.0195$ for the systems with soft and hard precipitates respectively. The choice was made such that the total volume of the precipitates was maintained constant for the CCE and CCI cases throughout the simulation. Hence, unlike the CC and CCE cases, there is no deviation in the coarsening kinetics in this comparison.

In Figure 14 (b), we show the evolution of R_{eff} of the smaller precipitate P_S for the CCED and CCID case with the edge connecting dislocation. The coarsening kinetics is accelerated for the case of harder precipitates and slowed down for the softer precipitates. As described in Section 4.5, both the dilatational and the deviatoric fields of the dislocations influence the solute flux in the precipitates. The solute flux is directed towards the dislocation in the case of the soft precipitate and away from the dislocation in the case of a hard precipitate. For the edge connecting dislocation, this creates a more prominent protrusion in the case of the soft precipitate as compared to the hard precipitate. Due to this, the concentration gradient between the precipitates is smaller (larger) in the case of the soft (hard) precipitates, resulting in the slower (faster) kinetics as compared to an elastically homogeneous system.

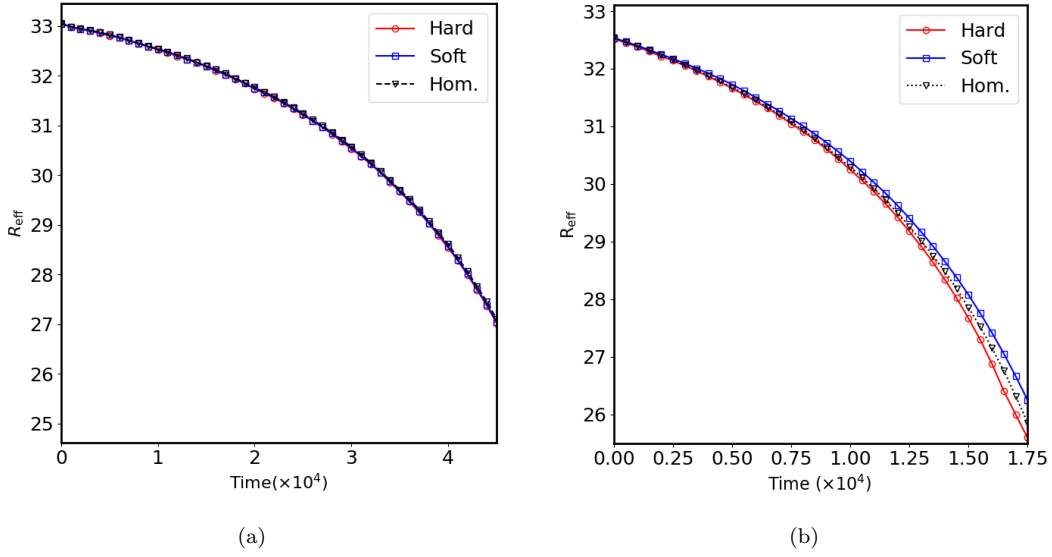


Figure 14. R_{eff} as a function of time for (a) CCE and CCI (hard and soft precipitate) cases (without dislocations and (b) CCED and CCID (Hard and soft precipitate) cases (with dislocations). The coarsening kinetics is identical for the CCE and CCI cases. It is clear from (b) that dislocations affect the coarsening kinetics differently for systems with hard or soft precipitates.

5. Conclusions

We have studied the effect of dislocations on coarsening of coherent precipitates using a phase field model that accounts for dislocation strain fields, pipe diffusion and coherency stresses and strains of solutes and precipitates.

We are able to capture the effect of pipe diffusion on accelerating the coarsening kinetics. In addition, when we incorporate the coherency effects, the driving force for coarsening is also affected. Specifically, the kinetics of coarsening becomes slower when the precipitates are connected by a dislocation segment of the edge type as compared to a case where we do not account for dislocation elastic fields. This is because the solutes in the precipitate find the dislocation elastic fields above the slip plane favourable and hence they set up a flux from below the slip plane to above the slip plane. This, in turn, decreases the equilibrium interfacial compositions outside the two precipitates, resulting in a smaller concentration gradient between them.

In addition, such fluxes driven by the solute-dislocation interactions alter the morphology of the coarsening precipitates; specifically, the nature of the dislocation and the elastic inhomogeneity play a role in determining the morphology. Since coarsening

is driven by curvature, the changes in morphology also affects coarsening rates.

In elastically inhomogeneous systems, the morphological changes are also affected by another phenomenon. The deviatoric components of the elastic fields do not interact with the precipitate fields when the elastic moduli of the system is homogeneous. However, in elastically inhomogeneous systems, with hard and soft precipitates, the interaction with the deviatoric fields of the dislocations cause a material build up / removal around the dislocation. This is true even for the case of the screw dislocation segment, in which the precipitate develops a protrusion (depression) at the point of exit of the dislocation, when the elastic moduli of the precipitate is harder (softer) as compared to the matrix phase.

We see that the modified Gibbs-Thomson equation, originally derived for an isolated precipitates in an infinite matrix, is also broadly applicable in the case of coarsening precipitates, situated at close proximity. Even in systems containing precipitates connected by dislocations, the change in the equilibrium interfacial composition calculated from modified Gibbs-Thomson equation using dislocation elastic fields from the simulation is close to that obtained from the composition profile.

For the same initial precipitate geometries, the coarsening kinetics remain the same for coherent precipitates as compared to the case where driving force due to interfacial curvature is only considered. In fact, we also note that the coarsening kinetics remain the same for the elastically homogeneous and inhomogeneous systems as well, in the absence of dislocations. However, in presence of dislocations, the elastically inhomogeneous systems behave differently as compared to a homogeneous system, with a system containing hard (soft) precipitates undergoing a faster (slower) coarsening kinetics.

Due to computational costs, in this study, we have only studied the coarsening of two coherent precipitates connected by a dislocation. A more realistic simulation of large number of particles would need a parallel implementation of the model.

Acknowledgement(s)

We thank (a) Dendrite and Space-Time, IIT Bombay, (b) Spinode – the DST-FIST HPC facility, Dept. of ME & MS, IIT Bombay, and (c) C-DAC, Pune for high per-

formance computing facilities. This project is funded by Science and Engineering Research Board, Dept. of Science and Technology, Govt. of India through the research grant CRG/2019/005060.

Disclosure statement

The authors declare that they have no known competing financial interests or personal relationships that could have appeared to influence the work reported in this paper.

References

- [1] D. A. Porter, K. E. Easterling, Phase transformations in metals and alloys (revised reprint), CRC press, 2009.
- [2] P. W. Voorhees, Ostwald ripening of two-phase mixtures, *Annual Review of Materials Science* 22 (1) (1992) 197–215.
- [3] I. M. Lifshitz, V. V. Slyozov, The kinetics of precipitation from supersaturated solid solutions, *Journal of Physics and Chemistry of Solids* 19 (1-2) (1961) 35–50.
- [4] C. Wagner, Theory of precipitate change by redissolution, *Zeitschrift für Elektrochemie* 65 (1961) 581–591.
- [5] A. J. Ardell, The effect of volume fraction on particle coarsening: theoretical considerations, *Acta Metallurgica* 20 (1) (1972) 61–71.
- [6] A. D. Brailsford, P. Wynblatt, The dependence of Ostwald ripening kinetics on particle volume fraction, *Acta Metallurgica* 27 (3) (1979) 489–497.
- [7] P. W. Voorhees, M. E. Glicksman, Ostwald ripening during liquid phase sintering—Effect of volume fraction on coarsening kinetics, *Metallurgical and Materials Transactions A* 15 (1984) 1081–1088.
- [8] J. A. Marqusee, J. Ross, Theory of Ostwald ripening: competitive growth and its dependence on volume fraction, *The Journal of Chemical Physics* 80 (1) (1984) 536–543.
- [9] Y. Enomoto, M. Tokuyama, K. Kawasaki, Finite volume fraction effects on Ostwald ripening, *Acta Metallurgica* 34 (11) (1986) 2119–2128.
- [10] W. C. Johnson, Precipitate shape evolution under applied stress—thermodynamics and kinetics, *Metallurgical and Materials Transactions A* 18 (1987) 233–247.

- [11] W. C. Johnson, On the elastic stabilization of precipitates against coarsening under applied load, *Acta Metallurgica* 32 (3) (1984) 465–475.
- [12] T. A. Abinandanan, W. C. Johnson, Coarsening of elastically interacting coherent particles—II. Simulations of preferential coarsening and particle migrations, *Acta Metallurgica et Materialia* 41 (1) (1993) 27–39.
- [13] W. C. Johnson, P. W. Voorhees, D. E. Zupon, The effects of elastic stress on the kinetics of Ostwald ripening: the two-particle problem, *Metallurgical Transactions A* 20 (1989) 1175–1187.
- [14] W. C. Johnson, T. A. Abinandanan, P. W. Voorhees, The coarsening kinetics of two misfitting particles in an anisotropic crystal, *Acta Metallurgica et Materialia* 38 (7) (1990) 1349–1367.
- [15] C.-H. Su, P. W. Voorhees, The dynamics of precipitate evolution in elastically stressed solids—I. Inverse coarsening, *Acta Materialia* 44 (5) (1996) 1987–1999.
- [16] G. Schmitz, P. Haasen, Decomposition of an Al–Li alloy—The early stages observed by HREM, *Acta Metallurgica et Materialia* 40 (9) (1992) 2209–2217.
- [17] Z. Wang, G. Shiflet, Growth of δ' on dislocations in a dilute Al–Li alloy, *Metallurgical and Materials Transactions* 29 (8) (1998) 2073–2085.
- [18] R. Monzen, K. Kita, Ostwald ripening of spherical Fe particles in Cu–Fe alloys, *Philosophical Magazine Letters* 82 (7) (2002) 373–382.
- [19] G. Shi, X. Chen, H. Jiang, Z. Wang, H. Tang, Y. Fan, Strengthening mechanisms of Fe nanoparticles for single crystal Cu–Fe alloy, *Materials Science and Engineering: A* 636 (2015) 43–47.
- [20] G. L. Dunlop, R. Honeycombe, The role of dislocations in the coarsening of carbide particles dispersed in ferrite, *Philosophical Magazine* 32 (1) (1975) 61–72.
- [21] S. Kuchler, V. Vojtech, S. S. Gerstl, R. E. Schäublin, J. F. Löffler, Thermally decomposed binary Fe–Cr alloys: toward a quantitative relationship between strength and structure, *Advanced Engineering Materials* 24 (3) (2022) 2100909.
- [22] W. C. Dash, Copper precipitation on dislocations in Silicon, *Journal of Applied Physics* 27 (10) (1956) 1193–1195.
- [23] R. Bullough, R. C. Newman, J. Wakefield, J. B. Willis, Precipitation on a dislocation, *Nature* 183 (4653) (1959) 34–35.
- [24] P. A. Beaven, E. P. Butler, Precipitate nucleation on dislocations in Fe–N, *Acta Metallurgica* 28 (10) (1980) 1349–1359.

- [25] W. Kesternich, Dislocation-controlled precipitation of TiC particles and their resistance to coarsening, *Philosophical Magazine A* 52 (4) (1985) 533–548.
- [26] Z. M. Wang, G. J. Shiflet, Heterogeneous nucleation of δ' on dislocations in a dilute Aluminum-Lithium alloy, *Metallurgical and Materials Transactions A* 27 (6) (1996) 1599–1609.
- [27] R. M. Allen, J. B. van Der Sande, A high resolution transmission electron microscope study of early stage precipitation on dislocation lines in Al-Zn-Mg, *Metallurgical Transactions A* 9 (1978) 1251–1258.
- [28] M. Zedalis, M. Fine, Precipitation and Ostwald ripening in dilute Al base-Zr-V alloys, *Metallurgical Transactions A* 17 (1986) 2187–2198.
- [29] L. Angers, M. E. Fine, J. R. Weertman, Effect of plastic deformation on the coarsening of dispersoids in a rapidly solidified Al-Fe-Ce alloy, *Metallurgical and Materials Transactions A* 18 (1987) 555–562.
- [30] M. Taneike, M. Kondo, T. Morimoto, Accelerated coarsening of MX carbonitrides in 12% Cr steels during creep deformation, *ISIJ International* 41 (Suppl) (2001) S111–S115.
- [31] T. Nakajima, M. Takeda, T. Endo, Accelerated coarsening of precipitates in crept Al-Cu alloys, *Materials Science and Engineering: A* 387 (2004) 670–673.
- [32] M. Legros, G. Dehm, E. Arzt, T. J. Balk, Observation of giant diffusivity along dislocation cores, *Science* 319 (5870) (2008) 1646–1649.
- [33] Y. Xia, X.-N. Luo, X.-Y. Zhong, H.-H. Zhou, C.-Y. Wang, J. Shi, In-situ TEM observation of cementite coarsening behavior of 5Mn steel during tempering, *Journal of Iron and Steel Research International* 23 (5) (2016) 442–446.
- [34] J. Lin, X.-N. Luo, X.-Y. Zhong, H.-H. Zhou, C.-Y. Wang, J. Shi, H. Dong, Dislocation pipe diffusion of Mn during annealing of 5-Mn steel, *Journal of Iron and Steel Research International* 23 (12) (2016) 1277–1280.
- [35] E. Tkachev, A. Belyakov, R. Kaibyshev, The role of deformation in coarsening of $M_{23}C_6$ carbide particles in 9% Cr Steel, *Physics of Metals and Metallography* 121 (2020) 804–810.
- [36] L.-Q. Chen, Phase-field models for microstructure evolution, *Annual Review of Materials Research* 32 (1) (2002) 113–140.
- [37] Y. Wang, J. Li, Phase field modeling of defects and deformation, *Acta Materialia* 58 (4) (2010) 1212–1235.
- [38] A. R. Varma, P. Pant, M. P. Gururajan, Dislocation assisted phase separation: A phase field study, *Acta Materialia* 244 (2023) 118529.

- [39] L. Lei, M. Koslowski, Mesoscale modeling of dislocations in molecular crystals, *Philosophical Magazine* 91 (6) (2011) 865–878.
- [40] A. Hunter, I. J. Beyerlein, T. C. Germann, M. Koslowski, Influence of the stacking fault energy surface on partial dislocations in FCC metals with a three-dimensional phase field dislocations dynamics model, *Physical Review B* 84 (14) (2011) 144108.
- [41] S. Y. Hu, L.-Q. Chen, A phase-field model for evolving microstructures with strong elastic inhomogeneity, *Acta Materialia* 49 (11) (2001) 1879–1890.
- [42] T. Mura, *Micromechanics of defects in solids*, Kluwer, 1987.
- [43] M. P. Gururajan, *Elastic inhomogeneity effects on microstructures*, Ph.D. thesis, Indian Institute of Science Bangalore (2006).
- [44] J. Zhu, L.-Q. Chen, J. Shen, V. Tikare, Coarsening kinetics from a variable-mobility Cahn-Hilliard equation: Application of a semi-implicit Fourier spectral method, *Physical Review E* 60 (4) (1999) 3564.
- [45] Y. Nishikawa, H. Jinnai, T. Koga, T. Hashimoto, S. T. Hyde, Measurements of interfacial curvatures of bicontinuous structure from three-dimensional digital images. 1. A parallel surface method, *Langmuir* 14 (5) (1998) 1242–1249.
- [46] A. R. Varma, *Effect of dislocations on phase separation and coarsening: a phase-field study*, Ph.D thesis to be submitted to IIT Bombay.
- [47] J. D. Eshelby, The determination of the elastic field of an ellipsoidal inclusion, and related problems, *Proceedings of the Royal Society of London. Series A. Mathematical and Physical Sciences* 241 (1226) (1957) 376–396.

Supplementary information

Calculation of farfield composition (c_f) for the CC case

For the CC case, the c_f is chosen as the equilibrium composition outside the precipitate for a precipitate of radius $R = 33$, obtained using the Gibbs-Thomson equation:

$$\Delta c_{int}^m = \frac{2\gamma\chi^p}{(c_\infty^p - c_\infty^m)\Psi_m} \quad (12)$$

In our simulations, the choice of parameters $A^{ch} = 1$ and $\kappa = 1$ lead to $\gamma = \frac{1}{3}$. As we consider a double-well potential with minima at $c_\infty^p = 1.0$ and $c_\infty^m = 0.0$, $c_\infty^p - c_\infty^m = 1.0$ (where c_∞ is the equilibrium composition for a system containing a flat interface.) $\Psi_m = \frac{\partial^2 f_0}{\partial c^2}$ is the curvature of the double-well potential at the matrix composition which is equal to 2 for the polynomial used as the double-well potential (and also equal to the curvature at the precipitate equilibrium composition). Therefore, eq. (12) becomes:

$$\Delta c_{int}^m = \frac{\chi^p}{3} \quad (13)$$

For the radius of $R = 33$, the mean curvature is given as: $\chi^p = \frac{1}{33}$. Hence, Δc_{int}^m is given as:

$$\Delta c_{int}^m = \frac{1}{99} = 0.0101 \quad (14)$$

Therefore, the composition outside the precipitate $c_{R=33}^m$ is given as:

$$c_{R=33}^m = c_{R=\infty}^m + 0.0101 = 0.0 + 0.0101 = 0.0101 \quad (15)$$

Calculation of farfield composition (c_f) for the CCE case

The farfield composition (c_f) for the CCE case is determined using the modified Gibbs-Thomson equation [10]:

$$\Delta c_{tot}^m = \frac{2\gamma\chi^p}{(c_\infty^p - c_\infty^m)\Psi_m} + \frac{\sigma_{ij}^m(\epsilon_{ij}^m - \epsilon_{ij}^p) + \frac{1}{2} [\sigma_{ij}^p(\epsilon_{ij}^p - \epsilon^c \delta_{ij}) - \sigma_{ij}^m \epsilon_{ij}^m]}{(c_\infty^p - c_\infty^m)\Psi_m} \quad (16)$$

In addition to the interfacial curvature contribution of Δc_{int}^m determined for the CC case, the equilibrium composition will also include an elastic contribution of Gibbs-Thomson equation, given by the second term. For the dilatational eigenstrain of magnitude $\epsilon^c = 0.01$ in an elastically homogeneous system corresponding to moduli parameters of $C_{44} = 140$ and $\nu = 0.294$, the stress and strain fields in the matrix and precipitate phases are obtained using the solution of the Eshelby inclusion problem [47] to be:

$$\sigma^m = \begin{bmatrix} -0.855556 & 0.0 & 0.0 \\ 0.0 & 0.427778 & 0.0 \\ 0.0 & 0.0 & 0.427778 \end{bmatrix} \quad (17)$$

$$\sigma^p = \begin{bmatrix} -0.855556 & 0.0 & 0.0 \\ 0.0 & -0.855556 & 0.0 \\ 0.0 & 0.0 & -0.855556 \end{bmatrix} \quad (18)$$

$$\epsilon^m = \begin{bmatrix} 0.006111 & 0.0 & 0.0 \\ 0.0 & 0.006111 & 0.0 \\ 0.0 & 0.0 & 0.006111 \end{bmatrix} \quad (19)$$

$$\epsilon^p = \begin{bmatrix} -0.0122222 & 0.0 & 0.0 \\ 0.0 & 0.006111 & 0.0 \\ 0.0 & 0.0 & 0.006111 \end{bmatrix} \quad (20)$$

From these values, the eq. (16) can be written as:

$$\Delta c_{tot}^m = 0.0101 + 0.0064 = 0.0165 \quad (21)$$

As the equilibrium composition for a system with a flat interface (that is, $R = \infty$) is $c_\infty^m = 0.0$, the equilibrium composition outside a precipitate of radius $R=33$ is given as:

$$c_R^m = c_\infty^m + 0.0165 = 0.0 + 0.0165 = 0.0165 \quad (22)$$

The farfield composition c_f for the CCI case was chosen as 0.0175 and 0.0195 for the cases with soft and hard precipitates, respectively, such that the total volume of the precipitates remain the same in the CCI and the CCE cases during coarsening, in order to compare the results from both cases.

Comparison of CC and CCE kinetics

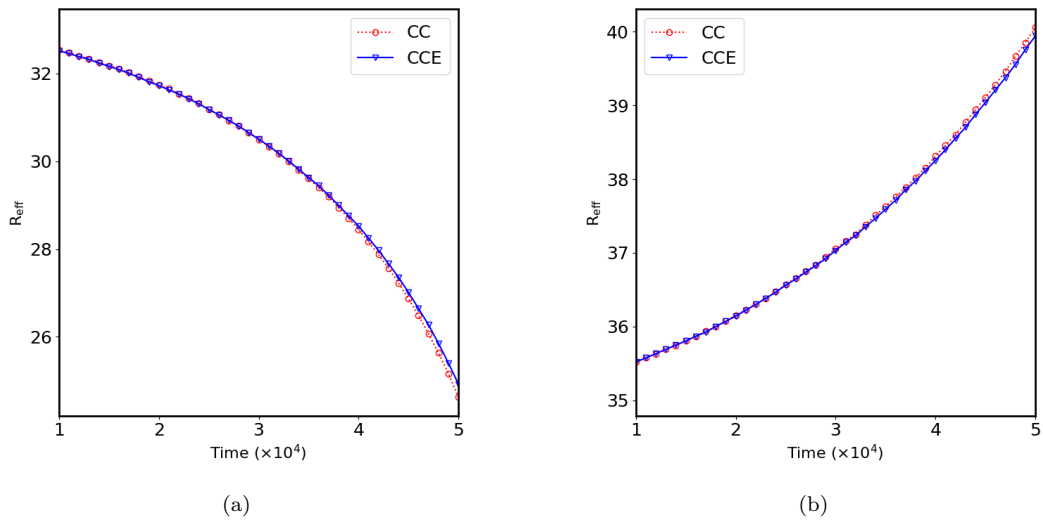


Figure 15. Effective radii of (a) P_S and (b) P_L as a function of time for the CC and the CCE cases. The initial adjustments upto $t=10000$ is not shown. The minor difference seen in the evolution of radii is due to the slight supersaturation of P_S in the CCE case.

Variable mobility due to pipe diffusion at dislocations

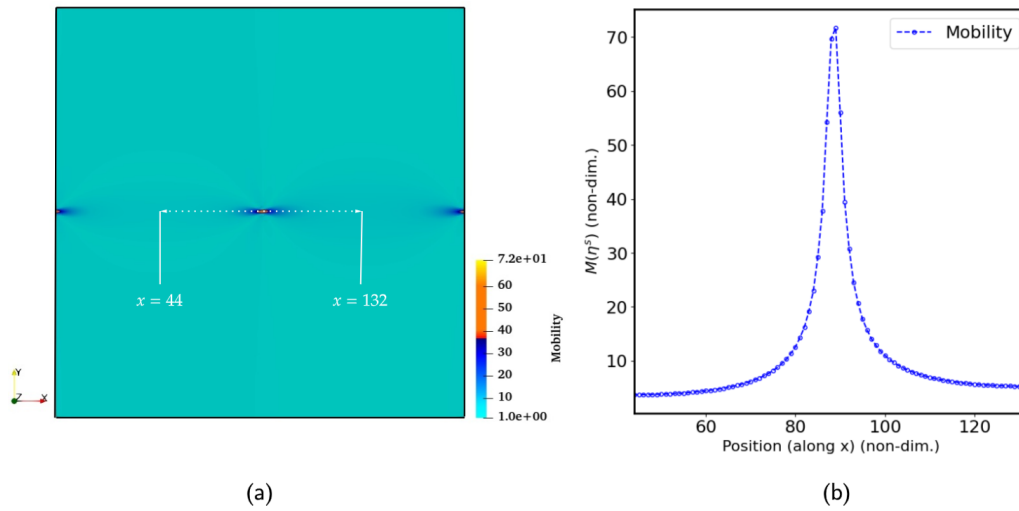


Figure 16. The mobility map plotted along the direction z , perpendicular to the slip plane of the dislocation. In (b), the mobility is plotted along the line shown in (a).